Journal of Applied Fluid Mechanics, Vol. 17, No. 3, pp. 628-645, 2024.
Available online at www.jafmonline.net, ISSN 1735-3572, EISSN 1735-3645.
https://doi.org/10.47176/jafm.17.3.2114

Hydrodynamic Performance of Cycloidal Propellers with Four-Bar and Mixed Four-bar/Five-bar Mechanisms: A Numerical Study

H. Yan, Z. Zhou, M. Lei, Z. Li and D. Xia†

School of Mechanical Engineering, Southeast University, Nanjing, Jiangsu, 211189, China

†*Corresponding Author Email: dxia@seu.edu.cn*

ABSTRACT

Cycloidal propellers constitute a specialized category of underwater propulsion devices, widely employed in vehicles requiring exceptional maneuverability. The parameters of the blade-driving mechanism directly impact the propeller performance. Hence, the effect of variations in the geometric parameters of the blade-driving mechanism on the hydrodynamic performance of cycloidal propellers must be investigated. In this study, a specific set of four-bar and mixed four-bar/five-bar mechanisms are taken as examples, and the effect of linkage-length variations on the hydrodynamic performance of cycloidal propellers was analyzed using numerical simulation methods. First, we established a physical model of the cycloidal propeller, and then derived the relationship between blade-rotation and revolution angles. Subsequently, by solving the Navier–Stokes equations and employing computational fluid dynamics simulations based on viscosity, an analysis is conducted to reveal the trends in the impact of different linkage-length combinations on the hydrodynamic performance of the cycloidal propeller. Finally, the outcomes of the numerical simulations are interpreted using the wing element theory. In similar blade-driving mechanisms, the effects of varying linkage lengths on propeller hydrodynamic performance are determined through alterations in the blade rotation angle range and equilibrium position. An increase in the range of the blade-rotation angle significantly enhances the hydrodynamic performance of the cycloidal propeller. This research employs a more realistic auto-propulsion mode for numerical simulations, establishing a mapping relationship between the blade-driving mechanism and hydrodynamic performance of the cycloidal propeller, while analyzing the underlying influencing mechanisms. Furthermore, crucial numerical simulations and theoretical foundations are employed for designing the four-bar and mixed four-bar/five-bar mechanism cycloidal propellers. The findings of this study could also be used in similar cycloidal propellers with multilinkage mechanism.

Article History

Received June 20, 2023
Revised October 9, 2023
Accepted October 18, 2023
Available online January 1, 2024

Keywords:

Cycloidal propeller
Four-bar mechanism
Mixed four-bar/five-bar mechanism
Numerical simulation
Self-propulsion

1. INTRODUCTION

As a critical component of marine engineering equipment and power positioning systems, underwater propellers directly determine the performance of power systems for marine engineering equipment. Commonly used underwater propellers include propeller thrusters, pump-jet propulsors, and biomimetic propellers. Among them, propeller thrusters are widely utilized owing to their simple structure and low cost in marine engineering applications (Bertram, 2012). Pump-jet propulsors generate thrust by using the reaction force of jetted water, significantly reducing noise during navigation (Qin et al., 2019). However, these two types of propellers can only generate propulsion in a single direction, thus requiring coordination using rudders at a certain speed to achieve vessel maneuverability. Biomimetic propellers imitate the propulsion of marine organisms, offering good maneuverability; however, their maximum power is constrained by their structural characteristics (Raj & Thakur, 2016). In addition, cycloidal propellers constitute a specialized category of underwater propulsion devices. Their unique motion mechanism enables them to produce thrust in any direction within the horizontal plane, allowing rapid and flexible adjustment of thrust magnitude and direction (Desai et al., 2020). This feature allows vehicles to achieve

NOMENCLATURE

C	chord length of the blades in van Manen's experiment	M_S	total torque on the cycloidal propeller
C_D	drag coefficient of the blade profile	$\boldsymbol{n}$	unit vector along the normal direction of ds
C_L	lift coefficient of the blade profile	n	revolution speed of the blade
D	rotational diameter of the blades	p	pressure
d	chord length of the blades	R	radius of the blade revolution
ds	differential unit area on the surface of the propeller blade	$\boldsymbol{u}$	fluid velocity vector
e	eccentricity of the cycloidal propeller	$\dot{\boldsymbol{\xi}}$	fluid boundary velocity
$\boldsymbol{F}$	fluid force acting on the vehicle	V_A	forward velocity of the cycloidal propeller
F_D	drag acting on the unit length of blade	V_R	resultant velocity of the blade motion
F_L	lift acting on the unit length of blade	W	blade thickness
F_S	total thrust on the cycloidal propeller	$\dot{\boldsymbol{x}}$	solid boundary velocity
J	advance coefficient		
K_D	thrust coefficient defined by Voith Company	δ	angle between the OX and XC bars in the five-bar mechanism
K_F	thrust coefficient defined by scientific research	ΔV	velocity difference
K_M	torque coefficient defined by scientific research	η	efficiency
K_S	torque coefficient defined by Voith Company	θ	revolution angle of the blade
L	extension length of the blades	θ'	angle between OC and OA' in the five-bar mechanism
L_a	length of a linkage in four-bar, mixed four-bar/five-bar mechanism	λ	advance coefficient (Voith Company)
L_b	length of a linkage in four-bar, mixed four-bar/five-bar mechanism	μ	dynamic viscosity
L_b'	equivalent length obtained by connecting point O and point C in the five-bar mechanism	ρ	density of the medium
L_c	length of a linkage in four-bar mechanism	$\overline{\overline{\boldsymbol{\sigma}}}$	normal stress tensor
L_{c1}	length of a linkage in one part of L_c in mixed four-bar/five-bar mechanism	φ	rotation angle of the blade
L_{c2}	length of a linkage in another part of L_c in mixed four-bar/five-bar mechanism	ω	blade revolution angular velocity
L_d	length of a linkage in four-bar, mixed four-bar/five-bar mechanism		
m	total mass of the vehicle	∇	gradient operator

lateral movement and pivot without requiring rudders. Simultaneously, these propellers can attain high rotation speeds to generate a greater power output. Their significance is particularly pronounced for vehicles, such as tugboats, and power positioning platforms operating in congested inland harbors (Voith, 2019). This novel capability has garnered considerable research attention and found extensive application in engineering projects.

The cycloidal propeller is designed based on the motion mechanism of "blades rotating around their own axis while revolving around a common axis, enabling them to meet the water flow at an appropriate angle." (Kirsten, 1922). Typically composed of 3–6 high aspect-ratio blades arranged parallel to the main axis, the cycloidal propeller's blades exhibit epitrochoid or hypocycloid pattern along their axis owing to their simultaneous rotation around the main axis while revolving. By adjusting the blades' self-rotation, the propeller can generate thrust in any direction within the vertical plane of its rotation axis (Jürgens et al., 2007). The kinematic behavior of each blade in the cycloidal propeller is governed by its blade-driving mechanism. Therefore, the design of the blade control mechanism constitutes a significant aspect of the overall propeller mechanism. The blade control mechanisms in the cycloidal propellers can be categorized into two main types: direct and mechanical controls. In the direct control approach, each blade is equipped with an individual control motor or hydraulic cylinder. However, owing to the revolution of the motor or hydraulic cylinder along with the blade, the complexity of the structural design increases (Valentini, 2001). Consequently, mechanical control mechanisms, such as those of gear, cam, and planar linkages, are more prevalent in practical applications. Among these, the planar linkage mechanism is prominent for its simplicity, compactness, and the flexibility to modify the blade rotation angle through adjustments in the linkage length. This confers significant engineering utility. Andrisani et al. (2016) demonstrated that from the perspective of unit power thrust analysis, the adoption of a sinusoidal motion pattern proves significantly advantageous for blade rotation. Based on fluid mechanics principles, further optimization of the blade's rotation pattern was conducted under hover conditions. The optimized motion pattern is relatively

complex but can be well-fitted using a four-bar mechanism to achieve a sinusoidal motion pattern for the blades. Based on the four-bar mechanism, Qian (1963) proposed a "mixed four-bar/five-bar mechanism" cycloidal propeller, which further reduces the vertical thickness of the propeller's driving mechanism. Laucks, R., & Blickle, (1983) developed a similar structural invention patent, which extended the engineering application of such cycloidal propulsion devices.

The theoretical research on cycloidal propellers has primarily focused on modeling methods and parameter optimization. To accurately obtain the hydrodynamic performance parameters of cycloidal propellers, researchers have proposed various calculation methods based on theories, such as the wing element theory (Wheatley & Windler, 1935), binary potential flow theory (Isay, 1968), ternary lift line theory (Brockett, 1991), momentum theorem (Bakhtiari & Ghassemi, 2019), and vortex theory (Yu et al. 2003). These methods explain the principles underlying the generation of thrust in cycloidal propulsion devices and predict their hydrodynamic performance to some extent. However, owing to the complexity of the flow field around cycloidal propellers, the prediction accuracy is limited. The widespread use of computers has facilitated the extensive application of computational fluid dynamics (CFD) methods (Li et al. 2023), which not only allow the calculation of transient performance of propellers but also significantly enhance the accuracy of performance predictions (Hafiz, 2023). Furthermore, CFD methods allow for detailed calculations of parameters related to vortices (Hu et al. 2022), thermodynamic performance (Amin et al. 2023), and other complex flow-field characteristics within the surrounding flow environment (Ju et al. 2022). In addition, numerical methods have been widely employed to optimize the performance and provide design guidance for cycloidal propellers. For instance, Shi et al. (2022) numerically analyzed unsteady vortex shedding and separation-induced transition of cycloidal propellers at low Reynolds numbers. Walther et al. (2019) investigated the impact of the asymmetric pitch of cycloidal propeller blades at ultra-low Reynolds numbers on propeller performance. Such studies delve into the intricate flow field within cycloidal propellers, explaining certain physical phenomena, although offering limited direct design guidance. Hu et al. (2019) optimized the aspect ratio and taper of cycloidal propeller blades in a hovering state. In another study, Jakson & José (2018) enhanced the overall performance of propellers by geometrically optimizing the blades and introducing harmonic vibrations. However, these investigations primarily concentrated on the blades or directly specified blade-rotation patterns, without considering the role of blade-driving mechanisms. In addition, numerical simulations often utilize incoming flow velocities to simulate propeller advancement or hovering, which is in contrast to the actual conditions of auto-propulsion of cycloidal propellers.

In this study, the effects of varying linkage lengths on the hydrodynamic performance of four-bar and mixed four-bar/five-bar cycloidal propellers were investigated. First, the physical model of the cycloidal propeller is established, and the corresponding rotation patterns of the blade's self-rotation are derived. In addition, the lengths of the linkage mechanisms to the blade's rotation angles were numerically derived. Subsequently, a viscosity-based CFD numerical simulation method, grounded in solving the Navier–Stokes equations, is utilized to comprehensively analyze the influence of different linkage lengths on the hydrodynamic performance of the cycloidal propeller. Finally, this study explores the effect of the linkage-length ratios on the thrust coefficient, torque coefficient, efficiency, and speed fluctuation during stable navigation for both four-bar and mixed four-bar/five-bar cycloidal propellers. This research bridges the gap between the hydrodynamic performance of the cycloidal propeller and the mechanical characteristics of the driving mechanism. Additionally, a more realistic auto-propulsion mode was employed for numerical simulations, offering crucial theoretical insights into the design of prototype cycloidal propellers with four-bar and four-bar/five-bar mechanisms.

2. METHODOLOGY

2.1 Computational Model

To numerically simulate cycloidal propellers with four-bar and four-bar/five-bar mechanisms to control a blade's rotation angle, a suitable numerical simulation model must be established for the cycloidal propeller. The propeller's body is designed in a cylindrical shape for the installation of components other than the blades of the cycloidal propeller. There are four blades installed beneath the body, the blade section being a NACA0030 aero foil, as shown in Fig. 1. We used the center of mass of the entire propeller as the origin and established an inertial coordinate system, *O-xyz*. Radius *R* of the blade revolution is a crucial dimension determining the thrust magnitude of the cycloidal propeller, and thus we adopt it as a reference dimension; we estimate the dimensions of components such as motors, servos, transmission mechanisms required for the physical model, and have selected the body's diameter and height as 2/3*R* and 18/5*R*, respectively. Furthermore, the axis of revolution of the cycloidal propeller coincides with the body's axis. To avoid the

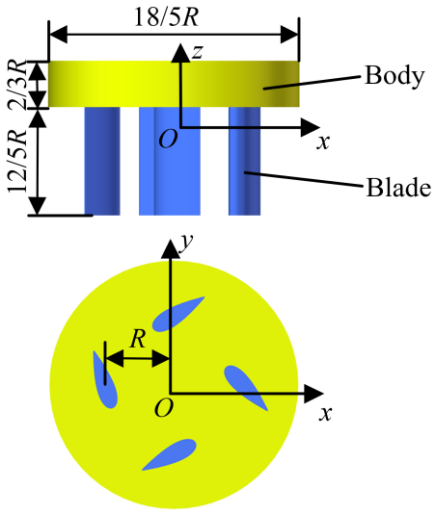

Fig. 1 Numerically simulated computational model of the cycloidal propeller

issue of insufficient thrust due to excessively short blades or the problem of bending caused by insufficient stiffness in overly long blades, the length of blade extension was set as $L = 12/5R$. When viewed from the negative direction of the z-axis, the blade revolves counterclockwise.

2.2 Kinematics Model

Various types of mechanisms can control the motion of cycloidal propeller blades, enabling simultaneous revolution and periodic self-rotation. This study focuses on two specific types of cycloidal propellers: the four-bar cycloidal propellers and mixed four-bar/five-bar cycloidal propellers. The mixed four-bar/five-bar mechanism is an evolution of the four-bar mechanism and serves as the blade control mechanism. Figure 2 provides a comparative illustration of the structures of the cycloidal propeller with four-bar and mixed four-bar/five-bar mechanisms. Figure 2(a) depicts the three-dimensional (3D) structure of the cycloidal propeller equipped with a four-bar mechanism.

As shown in Fig. 2(a), the four-bar mechanism comprises a control bar (1), revolution support (2), four connecting bars (3), and four blades (4). The revolution support adopts an "X" shape and is centrally mounted on the control bar, serving as the axis of revolution for the cycloidal propeller. Each extended end of the connecting bars is attached to a specific point on the chord line of the blades. The revolution support rotates around the rotational center, *O*, of the cycloidal propeller, inducing the blades to revolve around point *O*. One end of each of the four connecting bars is connected to a control point on the control bar, which differs from point *O*. The other end of each connecting bar is connected to a point on the chord line of the blade that is distinct from the connection point on the revolution support. The control point, also referred to as the eccentric point, is situated at distance *e* from point *O*, representing the eccentricity of this cycloidal propeller.

Owing to the necessity of connecting multiple linkages at the control point of the four-bar mechanism cycloidal propeller, the thickness inherently increases along the axial direction, posing a challenge to the overall structural design. Subsequently, the mixed four-bar/five-bar mechanism was derived based on the four-bar mechanism of the cycloidal propeller. The 3D structure of the cycloidal propeller with the mixed four-bar/five-bar mechanism is depicted in Fig. 2(b). The control bar (1), revolution support (3), and blades (5) in the cycloidal propeller with the mixed four-bar/five-bar mechanism remain the same as those used in the four-bar cycloidal propeller. However, the key distinction lies in the installation of a crossbar (2) at the control point on the control bar. This crossbar comprises one long end and three short ends. The long end is directly connected to the blade's chord line, thereby forming the four-bar mechanism. In contrast, the three short ends are connected to the blade's chord line via three connecting bars (4), thus forming the five-bar mechanism. This arrangement allows for the multiple links at the control point to be individually connected to the three short ends of the crossbar, thereby circumventing the issue of connecting all the linkages of the four-bar mechanism at a single point. Consequently, the axial space occupied by the driving mechanism of the cycloidal propeller is significantly reduced.

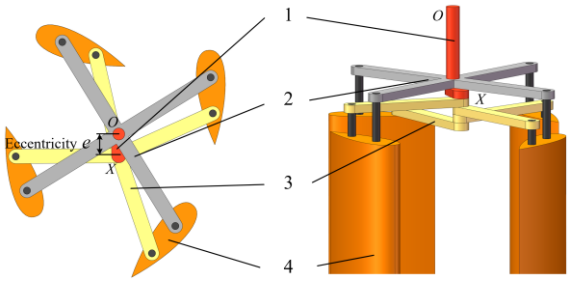

(a) Structural diagram of the four-bar mechanism cycloidal propeller

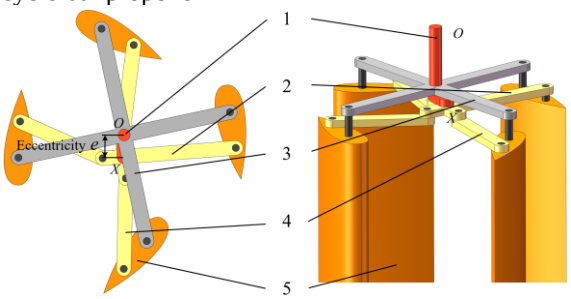

(b) Structural diagram of the cycloidal propeller with a mixed four-bar/five-bar mechanism

Fig. 2 Comparison of cycloidal propeller structures with a (a) four-bar and (b) mixed four-bar/five-bar mechanisms

Figure 3(a) and (c) depict a comparative illustration of the principles between the cycloidal propellers with four-bar and mixed four-bar/five-bar mechanisms. Figure 3(b) represents the planar schematic of a four-bar-mechanism cycloidal propeller with a single blade. A portion of the control bar (*OX*) a portion of the revolution support (*OA*) a connecting bar (*XB*), and a portion of the blade's chord length (*AB*) form the four connecting bars of the four-bar mechanism, as illustrated in Fig. 3(b). Here, *OX* serves as the frame, and *OA* functions as the driver arm. The driving torque of the cycloidal propeller acts upon the revolution support, driving the four blades in revolution. Simultaneously, under the influence of the control point and connecting bar, the blades rotate around rotation center *A*. In Fig. 3(b), θ and φ represent the revolution and rotation angles of the blade, respectively. *OA* rotates counterclockwise with an angular velocity of ω. Assuming that the lengths of the four bars in the four-bar mechanism are denoted as L_a, L_b, L_c, and L_d, by drawing perpendicular lines from point *X* and *B* to *OA*, the geometric relationship can be used to derive the relationship between θ and φ:

$$\begin{aligned}&(L_d \sin\varphi - L_b \sin\theta)^2 + \\ &(L_a - L_b \cos\theta + L_d \cos\varphi)^2 = {L_c}^2\end{aligned} \tag{1}$$

Through derivation, we obtained the corresponding values of φ for different angles, θ, representing the relationship between the rotation and revolution angles of the blade of the four-bar mechanism. As shown in Fig. 3(a), the structure of the four-bar mechanism driving each blade, frame position, and lengths of the connecting bars are identical in the four-bar mechanism cycloidal propeller. Therefore, the rotation patterns of each blade can be described using Eq. (1) with the addition of a phase difference.

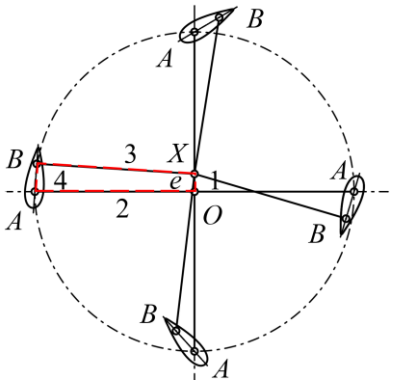

(a) Schematic of the cycloidal propeller with a four-bar mechanism

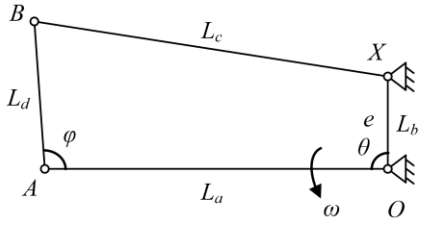

(b) Plan view of single blade four-bar control mechanism

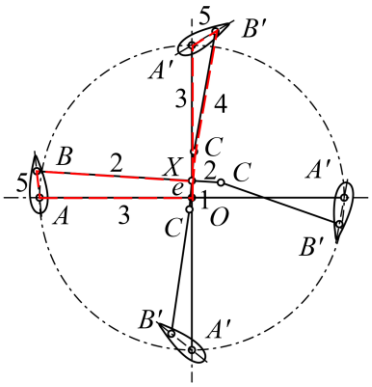

(c) Schematic of the cycloidal propeller with a mixed four-bar/five-bar mechanism

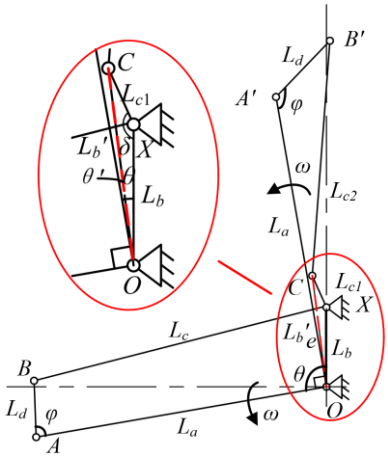

(d) Plan view of a single blade mixed four-bar/five-bar control mechanism

Fig. 3 Comparison of the principles of (a and b) four-bar and (c and d) mixed four-bar/five-bar cycloidal propellers

Figure 3(d) depicts the planar schematic of the cycloidal propeller with a single blade driven by the mixed four-bar/five-bar mechanism. The diagram shows the principle similar to the previous explanation, where the long end of the crossbar corresponds to the blade driven by the four-bar mechanism, denoted as *OXBA*. During the rotation of the four-bar mechanism, the *XB* bar functions as the follower arm, and guided by the crossbar and active arm *OA*, the arm rotates in a specific pattern. The three short ends of the crossbar correspond to the three blades, forming a five-bar mechanism, denoted as *OXCB'A'*. This mechanism comprises a portion of the control bar (*OX*), the short end of the crossbar (*XC*), the connecting bar (*CB'*), a segment of the blade's chord length (*A'B'*), and a portion of the revolution support (*OA'*). Within the five-bar mechanism, *OA'* and *XC* function as the active arms, with *OA'* being a component of the revolution support and rotating around point *O* with an angular velocity of ω. The rotation of *XC* is determined by the motion of the four-bar mechanism and the geometric structure of the crossbar, both of which collectively determine the movement characteristics of the five-bar mechanism. Together, they drive the blade, while it revolves, to undergo periodic rotation around point *A'*.

The five-bar mechanism is essentially obtained by dividing the L_c bar of the four-bar mechanism into two parts. Let L_a, L_b, L_{c1}, L_{c2}, and L_d represent the lengths of the five bars in the five-bar mechanism as shown in Fig. 3(c). Consider an example of a blade driven by a five-bar mechanism, let δ be the angle between the *OX* and *XC* bars, we obtain the structure shown in Fig. 3(d). By connecting points *O* and *C* in the five-bar mechanism, *OC*, *CB'*, *A'B'*, and *OA'* form a four-bar mechanism. Through derivation, the following relationship is obtained:

$$(L_d \sin\varphi - L_b' \sin\theta')^2 + (L_a - L_b' \cos\theta' + L_d \cos\varphi)^2 = L_{c2}^2 \tag{2}$$

where θ' and L_b' can be obtained by solving triangle *OXC*:

$$L_b' = \sqrt{L_b^2 + L_{c1}^2 - 2L_b L_{c1}\cos\delta} \tag{3}$$

$$\theta' = \theta - \arcsin\left(\frac{L_{c1}\sin\delta}{L_b'}\right) \tag{4}$$

Accordingly, the relationship between the rotation angle of the blade driven by the five-bar mechanism and the revolution angle can be obtained. The motion patterns of the remaining two blades can be derived by considering the change in angle δ, which is determined by the crossbar structure. The derivation process follows the same procedure as described earlier.

In hydrodynamic numerical simulation of cycloidal propellers, several important dimensionless evaluation indices were introduced to assess the hydrodynamic performance of the propulsion device. These include are

the advance coefficient, thrust coefficient, and torque coefficient. The Voith Company (2021) provides the following definitions for these three parameters:

$$\left.\begin{aligned} \lambda &= \frac{V_A}{\pi n D} \\ K_S &= \frac{2F_S}{\pi^2 \rho L n^2 D^3} \\ K_D &= \frac{4M_S}{\pi^2 \rho L n^2 D^4} \end{aligned}\right\} \tag{5}$$

In the equation, λ, K_S, and K_D represent the coefficients of advance, thrust, and torque defined by Voith Company, respectively. In addition, V_A denotes the forward velocity of the cycloidal propeller, n represents the revolution speed, D is the revolution diameter of the blades, F_S and M_S are the total thrust and torque exerted on the cycloidal propeller, respectively. Furthermore, ρ represents the density of the medium (in this study, water) and L represents the blade span.

In scientific research, it is common practice to analogously adjust the hydrodynamic performance parameters of propellers by multiplying the parameters in Eq. (5) by a certain coefficient, yielding the key parameters for evaluating the hydrodynamic performance of cycloidal propellers as shown in Eq. (6).

$$\left.\begin{aligned} J &= \frac{V_A}{R\omega} \\ K_F &= \frac{F_S}{\rho \omega^2 R^4} \\ K_M &= \frac{M_S}{\rho \omega^2 R^5} \end{aligned}\right\} \tag{6}$$

where J represents the advance coefficient, K_F represents the thrust coefficient, and K_M represents the torque coefficient. Furthermore, ω and R denote the revolution angular velocity and radius of the blade.

In addition, propulsion efficiency η of the vehicle is introduced to evaluate its overall performance:

$$\eta = \frac{F_S V}{M_S \omega} \tag{7}$$

By introducing Eq. (6) into Eq. (7) and simplifying it, we can conclude that

$$\eta = \frac{J K_F}{K_M} \tag{8}$$

When the underwater vehicle propelled by the cycloidal propeller accelerates to a stable average velocity over multiple cycles, it is considered to have entered the steady-state navigation phase. The aforementioned parameters were calculated based on the values obtained during this steady-state navigation phase.

In addition to the three aforementioned parameters, the autonomous navigation of a vehicle propelled by a cycloidal propeller must be analyzed for the smoothness of navigation. This refers to the fluctuation of propulsive force generated by the cycloidal propeller during each revolution cycle, after the vehicle enters the steady-state navigation phase. In this study, the difference in forward velocity within one cycle of the steady-state navigation, denoted as ΔV, is used as a measure. The smaller the value of ΔV, the smaller the fluctuation of vehicle velocity within a cycle, indicating better stability in the generation of propulsive force by the cycloidal propeller.

2.3 Control Equations, Numerical Simulation Methods and Computational Grids

With the maturation of CFD methods, their application enables an accurate and efficient prediction of the hydrodynamic performance of cycloidal propellers, thus saving a significant amount of time and material costs associated with experimental testing (Bakhtiari & Ghassemi, 2020). Therefore, in this study, the CFD method was adopted to perform numerical simulations of cycloidal propellers.

This study focused on the self-propulsion of underwater vehicles in a 3D flow. The Navier–Stokes equations are solved using the finite volume method, where spatial discretization is performed using a Green–Gauss cell-based approach for gradient interpolation. The second-order central differencing scheme was employed to calculate the velocity and pressure gradients on the computational grid. The discretization of the Navier−Stokes equations by using the finite volume method can be described as follows:

$$\nabla \cdot \boldsymbol{u} = 0 \tag{9}$$

$$\rho \frac{\partial \boldsymbol{u}}{\partial t} + \rho(\boldsymbol{u} \cdot \nabla)\boldsymbol{u} = -\nabla p + \mu \nabla^2 \boldsymbol{u} \tag{10}$$

where $\boldsymbol{u}$ is the fluid velocity vector, ρ is the density, p is the pressure, μ is the dynamic viscosity, and ∇ is the gradient operator. In this study, the coupled algorithm based on pressure solving was employed to calculate the pressure–velocity coupling in the continuity equation. In addition, the Reynolds-averaged Navier–Stokes (RANS) model was used to perform time-averaged numerical computations of the flow field around the cycloidal propeller at various Reynolds numbers.

To solve the equations within the moving domain, a no-slip boundary condition must be imposed on the surface of the structure, which ensures that fluid velocity $\dot{\boldsymbol{\xi}}$ is equal to the solid boundary velocity, $\dot{\boldsymbol{x}}$.

$$\dot{\boldsymbol{\xi}} = \dot{\boldsymbol{x}} \tag{11}$$

The motion of an underwater vehicle in water can be described by Newton's second law as follows:

$$m\ddot{\boldsymbol{x}} = \boldsymbol{F} \tag{12}$$

where $\boldsymbol{F}$ represents the fluid force acting on the cycloidal-driven underwater vehicle, and m denotes the total mass of the vehicle. Fluid force $\boldsymbol{F}$ can be expressed as follows:

$$\boldsymbol{F} = \int_S \overline{\overline{\boldsymbol{\sigma}}} \cdot \boldsymbol{n} ds \tag{13}$$

where $\overline{\overline{\boldsymbol{\sigma}}}$ is the normal stress tensor, ds is the differential unit area on the surface of the propeller blade, and $\boldsymbol{n}$ is the unit vector along the normal direction of ds.

In this study, the flow field is divided into inner and outer domains near and farther away from the underwater

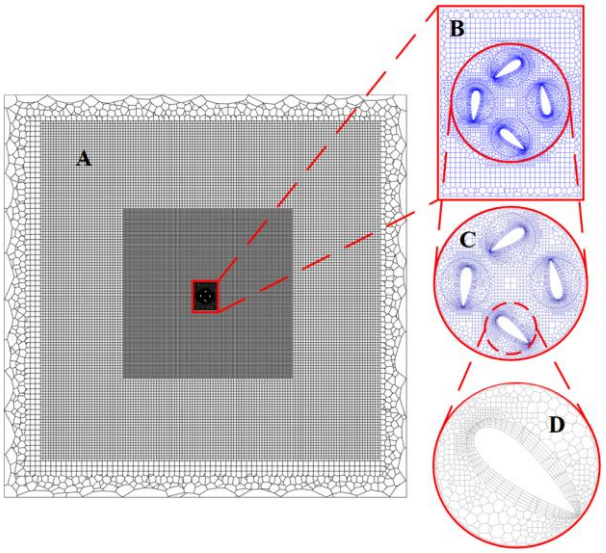

Fig. 4 Computational domain and grid

vehicle, respectively. The rotation of the cycloidal propeller blade, the forward movement of the vehicle, and the solution of the Newton's motion equations were implemented using user-defined functions (UDFs). During the transient solution process, to achieve the autonomous motion of the underwater vehicle driven by the cycloidal propeller, UDFs are called at each time step to define the overall translational and rotational motions of the shared contact surface between the outer and inner domains. Additionally, another UDF was used to define the custom motion of the grid region. The motion laws of the revolution and rotation of the cycloidal propeller blade are implemented using the sliding mesh method. All dynamic results, including acceleration, velocity, and displacement, are computed using Eq. (12). To ensure the connectivity between the inner and outer domains, a dynamic mesh and sliding mesh techniques were employed in the outer domain. These techniques ensure that the shared contact surface between the outer and inner grids moves at the same velocity, achieving a real-time docking effect at the interface between the outer and inner domains.

The computational domain and grid used in this study are shown in Fig. 4. The computational domain is a cubic water tank with dimensions of 4 m × 4 m × 1 m. In addition, the boundary conditions were set for the computational domain, with the right side of the tank set as a pressure outlet, and the remaining sides set as no-slip wall conditions. The entire computational domain was divided into four regions, namely A, B, C, and D, from the outer to inner domains, for numerical simulation. Region A represents the outer flow domain, region B represents the inner flow domain, region C represents the cycloidal propeller section, and region D represents the blade section. To facilitate the grid restructuring during the dynamic mesh process, the grid in the outer flow domain, A, was set as unstructured, while in the inner flow domain, B, and the sections of the cycloidal propeller C and blades D, the sliding mesh technology was applied, thus utilizing hexahedral structured grids. To enhance computational accuracy, local grid refinement was implemented in the blade region of the propeller to improve the calculation precision.

Table 1 Validation parameters for numerical simulation

Parameter Name	Parameter Value
Rotational diameter D	200 mm
Number of blades	4
Blade spreading length L	0.6 D
Blade chord length C	0.18 D
Blade thickness W	0.026 D
Blade shape	Rectangle
Blade section profile	Symmetries
Blade motion	Cycloidal motion
Eccentricity	0.5
Rotational speed	6 rps
Reynolds number	1.4×10^5

2.4 Validation of Numerical Simulation Effectiveness

To validate the accuracy of the proposed numerical simulation method, the numerical results of the hydrodynamic performance of the cycloidal propeller were compared with that of the experimental data. Manen (1966) conducted comprehensive experimental research on the thrust coefficient, torque coefficient, and efficiency of a 4-blade cycloidal propeller.

Therefore, this study adopted the above-mentioned modeling method, and the geometric parameters were set to the same values as in Van Manen's experiments, as shown in Table 1. Rectangular blades with symmetric NACA 4-digit profiles were used, and multiple sets of numerical simulations were performed by varying the advance coefficient. Note that the cycloidal propeller used in Van Manen's experiments employed normal-orthogonal motion patterns. Therefore, we used the same normal-orthogonal motion patterns for verifying blade rotation.

The numerically obtained thrust coefficient, torque coefficient, and efficiency were compared with Van Manen's experimental data, and the comparison curves are shown in Fig. 5. The figure reveals a close match between both the results in terms of various hydrodynamic performance parameters. The values are in close proximity, exhibiting similar trends, and overall consistency with the experimental findings. Therefore, the proposed numerical method to predict the hydrodynamic performance of the cycloidal propeller can be considered reliable.

3. RESULTS

3.1 Determination of Linkage Length for the Four-Bar Cycloidal Propellers

In designing a four-bar cycloidal propeller, appropriate lengths of the four linkages, namely L_a, L_b, L_c, and L_d must be initially selected. Among these, L_a determines the revolution radius of the propeller blades, and is itself calculated based on the dimensions of the mechanism and design requirements. To enhance the

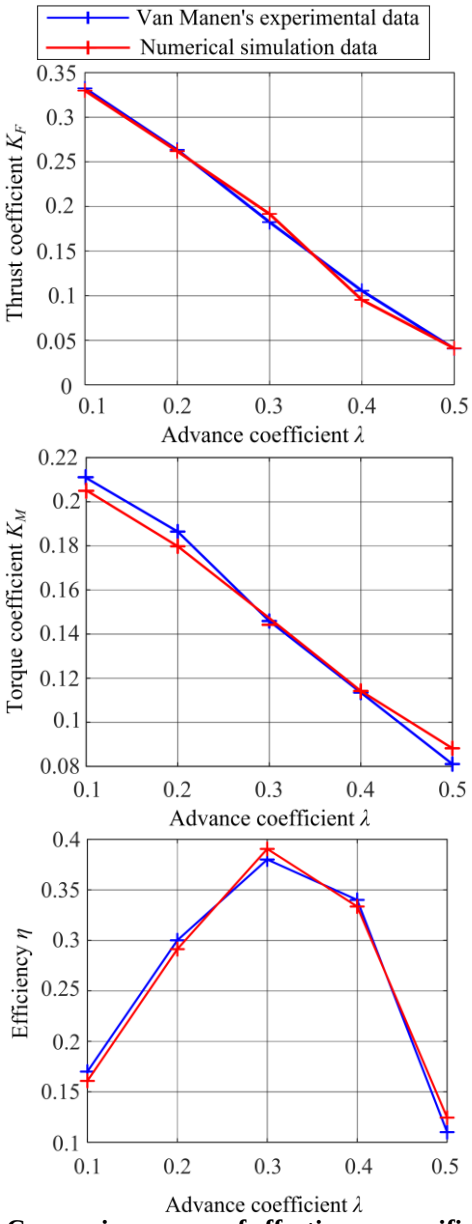

Fig. 5 Comparison curve of effectiveness verification

generality of this research, the lengths of the remaining linkages are provided as ratios with respect to the revolution radius, R. In this study, considering factors such as maximum available motor power, convenience of component manufacturing and assembly, the revolution radius of the blades was determined as R = 45 mm. Therefore, L_a was set as R = 45 mm.

In the design of conventional four-bar cycloidal propellers, the number of variables is generally reduced by imposing additional constraints on the four-bar mechanism. In general, when L_b = 0, indicating that the control point of the cycloidal propeller mechanism coincides with the axis of rotation, the propeller does not generate thrust. This condition implies that the rotational angles of the four blades are all 0°. Under this requirement, the geometric relationship can be derived as $L_c^2 = L_a^2 + L_d^2$. By introducing this constraint, the length of L_c can be determined by the values of L_a and L_d. Therefore, only lengths L_b and L_d must be determined.

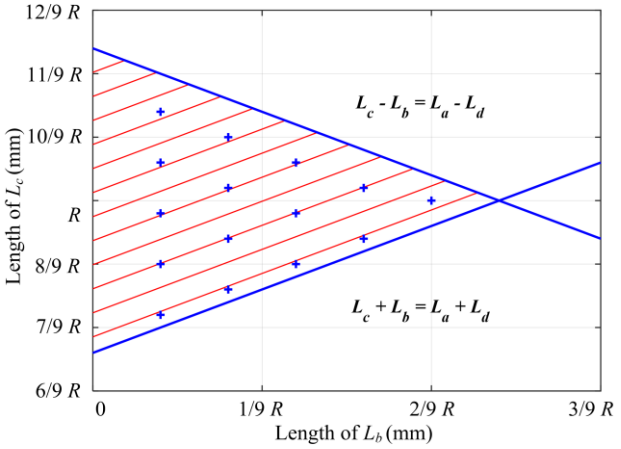

Fig. 6 Illustration of the range of values for lengths, L_b and L_c

Furthermore, considering that the L_d bar in the four-bar mechanism represents a portion of the blade's chord length, and given that the chord length itself has a limited range of variation, the proposed approach initially sets L_d as a constant. Based on the determined values of L_a and L_d, the study first investigated the influence of variations in L_b and L_c on the hydrodynamic performance of the cycloidal propeller. After determining the values of L_b and L_c, the impact of varying L_d on the performance of the cycloidal propeller was examined.

According to the principles of mechanics, in a four-bar mechanism, where the lengths of two linkages are determined, the lengths of the other two linkages must satisfy the following condition:

$$\left.\begin{aligned} &L_c + L_b < L_a + L_d \\ &L_c - L_b > L_a - L_d \\ &L_b > 0\ ,\ L_c > 0 \end{aligned}\right\} \tag{14}$$

To provide more options for L_b and L_c, while considering the limitation of the blade chord length, the initial value of L_d was selected as 4/15R = 12 mm. By substituting $L_a = R$ = 45 mm, the values of L_b and L_c were plotted on the x- and y-axes, respectively. The shaded region in Fig. 6 represents the range of values for the points that satisfy the inequality in Eq. (14).

As shown in Fig. 6, 15 points represented by "+" were uniformly selected. The L_b and L_c lengths were used to plot the coordinates of these points, resulting in the construction of a cycloidal propeller with the four-bar mechanism, as described in Section 2.1. Under the numerical simulation conditions described in Section 2.3, a self-propelled numerical simulation of the cycloidal propeller-driven underwater vehicle was conducted with a rotational speed of 5 rps, as shown in Fig. 7 with symbol "+." For the convenience of data analysis, a least squares method was used to fit the data points to 3D planes. The equations of the fitted planes are listed in Table 2.

Figure 7(a) presents the variations in the thrust coefficient with respect to L_b and L_c. As shown, within the linkage-length range considered in the numerical simulation, the thrust coefficient shows a monotonically

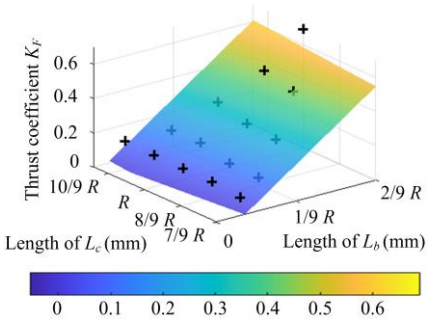

(a) Variation in the thrust coefficient with respect to lengths L_b and L_c

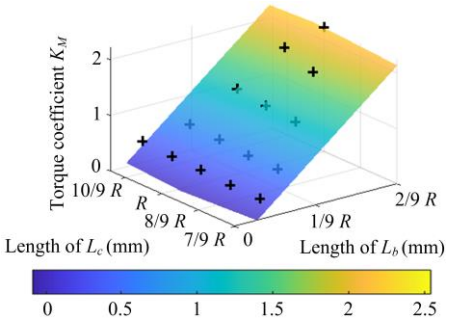

(b) Variation in the torque coefficient with respect to lengths L_b and L_c

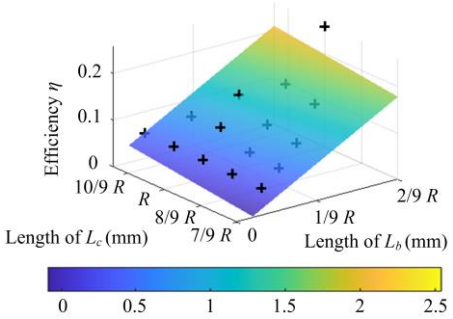

(c) Variation in efficiency with lengths L_b and L_c

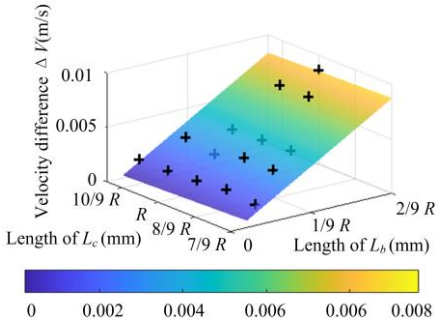

(d) Variation of maximum velocity difference within one cycle with lengths L_b and L_c

Fig. 7 Variations in the performance parameters of the four-bar cycloidal propeller with lengths L_b and L_c

increasing trend along the positive *x*-axis (i.e., in the direction of increasing L_b) and along the positive *y*-axis (i.e., in the direction of increasing L_c). The comparison of the coefficients in the corresponding fitted-plane equations (Table 2) demonstrates that the slope of the fitted plane along the positive *x*-axis is significantly

Table 2 Data point fitting plane equation shown in Fig. 7

Figure number in Fig. 7	Performance parameter	Fitting plane equations
Fig. 7(a)	Thrust coefficient K_F	$z = 0.06659x + 0.00385y - 0.2554$
Fig. 7(b)	Torque coefficient K_M	$z = 0.24680x + 0.00946y - 0.6683$
Fig. 7(c)	Efficiency η	$z = 0.01940x + 0.00196y - 0.0851$
Fig. 7(d)	Velocity difference ΔV	$z = 0.00090x - 0.00002y + 0.0006$

greater than the slope along the positive *y*-axis. This indicates that increasing both L_b and L_c will result in an increase in the thrust coefficient of the cycloidal propeller. However, the effect of L_b variation on the thrust coefficient is more pronounced than that of L_c variation. To achieve a higher thrust coefficient, a combination of larger values of L_b and L_c is recommended. In the selected dataset, L_b should be set to 2/9*R* (10 mm) and L_c should be set to *R* (45 mm).

Figure 7(b) presents the variations in the torque coefficient with respect to L_b and L_c. As shown, within the range of linkage lengths considered in the numerical simulation, the torque coefficient shows a monotonically increasing trend along the positive *x*-axis (i.e., in the direction of increasing L_b) and along the positive *y*-axis (i.e., in the direction of increasing L_c). The comparison of the coefficients in the corresponding fitted-plane equations (Table 2) demonstrated that the slope of the fitted plane along the positive *x*-axis is significantly greater than the slope along the positive *y*-axis. This indicates that an increase in both L_b and L_c would increase the torque coefficient of the cycloidal propeller. However, the effect of L_b variation on the torque coefficient is more pronounced than that of L_c variation. In practical applications, to generate greater propulsion force while minimizing the resistance moment, a combination of smaller L_b and L_c values must be selected. In the dataset selected in this study, L_b should be set to 2/45*R* (2 mm) and L_c should be set to 4/5*R* (36 mm). This conclusion differs from that shown in Fig. 7(a); therefore, further analysis of the efficiency of the cycloidal propeller system is required to make a final judgment.

Figure 7(c) illustrates the variation in the efficiency of the cycloidal propeller with respect to L_b and L_c. Similar to Fig. 7(a) and 7(b), the efficiency of the cycloidal propeller exhibits a monotonic increasing trend with increasing values of L_b and L_c. The comparison of the coefficients before *x* and *y* in the corresponding fitting plane equations in Table 2 showed that the slope of the fitting plane along the *x*-axis is significantly larger than the slope along the *y*-axis. This indicates that an increase in both linkage lengths, L_b and L_c, increases the efficiency of the cycloidal propeller. However, variations in L_b display a more pronounced effect on the efficiency of the cycloidal propeller than variations in L_c. To achieve higher efficiency, a combination of larger values of L_b and L_c must be selected. Therefore, based on the data considered

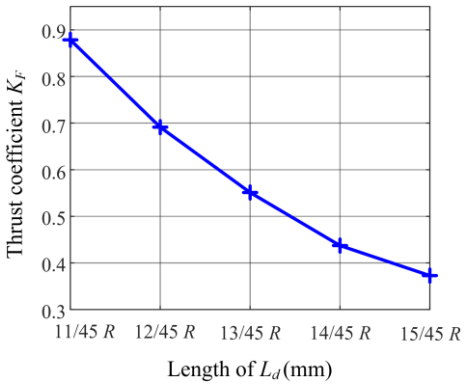

(a) Variation in the thrust coefficient with length L_d

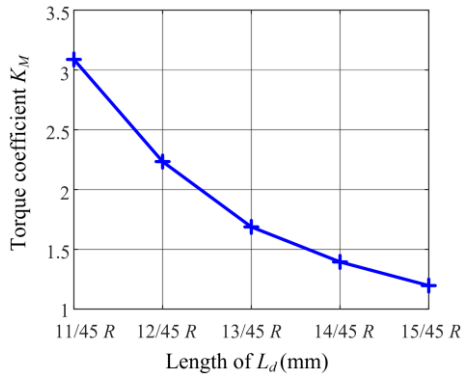

(b) Variation in the torque coefficient with length L_d

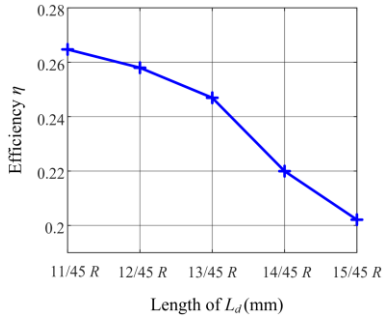

(c) Variation in the efficiency with length L_d

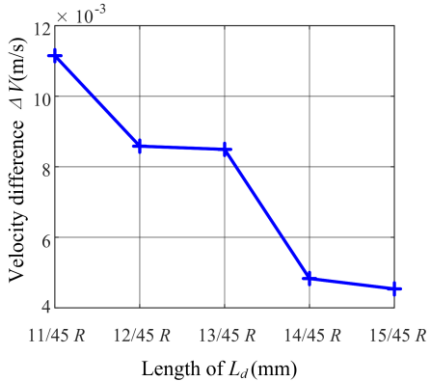

(d) Variation of maximum velocity difference within one cycle with respect to length L_d

Fig. 8 Variation of performance parameters of the four-bar cycloidal propeller with respect to L_d

in this study, L_b should be set to 2/9R (10 mm) and L_c should be set to R (45 mm).

Figure 7(d) presents the variation of the maximum velocity difference within one cycle of stable navigation for the self-propelled cycloidal propeller with respect to L_b and L_c. The graph and equations of the fitting plane show that the fluctuation within one cycle of the cycloidal propeller after stabilization increases slightly with the increase of L_b, while the variation in L_c is not significant. The coefficients of the fitting plane are several orders of magnitude smaller than the coefficients of the fitting planes of thrust force, torque moment, and efficiency. Therefore, considering the numerical simulation data selected in this study, the velocity difference within one cycle after stabilization of the cycloidal propeller is minimally affected by L_b and L_c.

Accordingly, the linkage-length combination of L_b = 2/9R = 10 mm and L_c = R = 45 mm was selected to further study the value of linkage length, L_d, in the four-bar cycloidal propeller. In addition, considering the geometric relationship of the three linkage lengths determined for the four-bar mechanism and the practical situation of the blade chord length in the cycloidal propeller, L_d was varied as 11/45R, 12/45R, 13/45R, 14/45R, and 15/45R for numerical simulations. Figure 8 shows the obtained results.

Moreover, Fig. 8(a), (b), and (c) respectively illustrate the variation in the coefficients of thrust force, torque, and the efficiency of the four-bar cycloidal propeller with respect to the linkage length, L_d. As shown, with the increase in L_d, the thrust coefficient, torque coefficient, and efficiency exhibit a monotonically decreasing trend. In the data considered in this study, the maximum values of the thrust coefficient, torque moment coefficient, and efficiency are achieved when L_d = 11/45R = 11 mm. Therefore, from an efficiency perspective, a smaller value of L_d should be selected for the four-bar cycloidal propeller. The validated data present the optimal linkage lengths for the four-bar mechanism as L_a = R = 45 mm, L_b = 2/9R = 10 mm, L_c = R = 45 mm, and L_d = 11/45R = 11 mm, resulting in the highest efficiency for the cycloidal propeller. Figure 8(d) shows that with the increase in L_d, the velocity difference within one cycle during stable navigation decreases; however, the magnitude of the decrease is very small. Therefore, we can conclude that the velocity difference within one cycle after stabilization of the cycloidal propeller is minimally affected by L_d, which is only slightly affected by the selection of appropriate linkage lengths.

3.2 Determination of Linkage Length for Mixed Four-Bar/Five-Bar Cycloidal Propellers

Based on the determination of the influence of varying linkage lengths on the four-bar cycloidal propeller on the hydrodynamic performance, the effect of linkage lengths on the mixed four-bar/five-bar cycloidal propeller on the hydrodynamic performance. As analyzed in Section 2.2, the mixed four-bar/five-bar mechanism is an improved version of the four-bar mechanism, with the main difference being the division of L_c into L_{c1} and L_{c2}, forming the five-bar mechanism. Therefore, based on the linkage lengths determined in Section 3.1 for the four-bar mechanism, further research was conducted on the impact

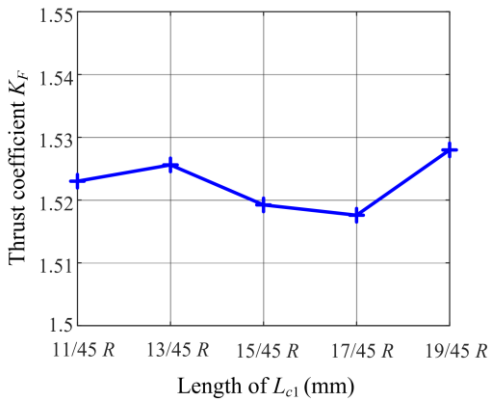

(a) Variation of thrust coefficient with respect to length L_{c1}

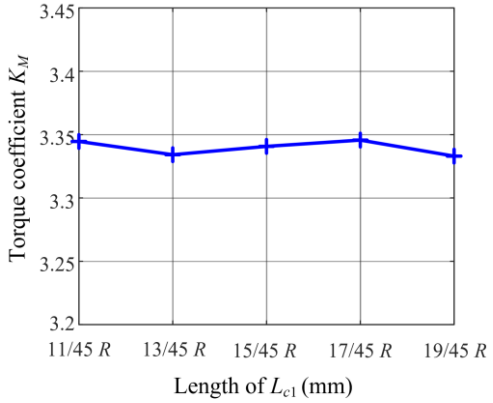

(b) Variation of torque coefficient with respect to length L_{c1}

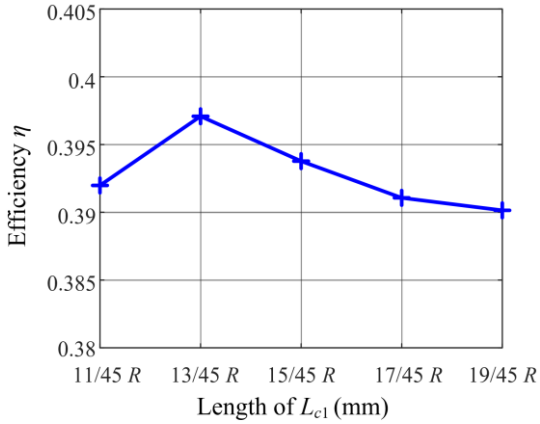

(c) Variation of efficiency with respect to length L_{c1}

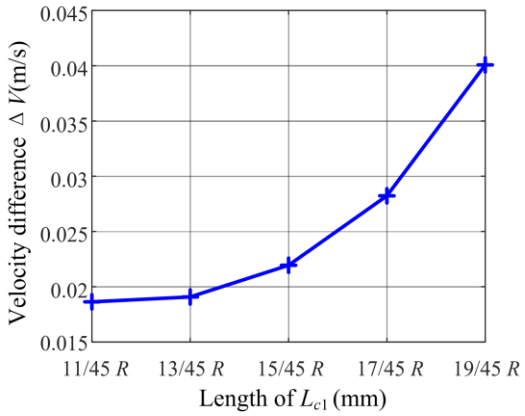

(d) Variation of the maximum velocity difference within one cycle with respect to length L_{c1}

Fig. 9 Variations in the performance parameters of the four-bar cycloidal propeller with respect to L_{c1}

of dividing L_c on the hydrodynamic performance of the mixed four-bar/five-bar cycloidal propeller.

The four-bar mechanism was modified into the five-bar mechanism mainly to reduce the vertical installation thickness of the cycloidal propeller. Considering the installation dimensions, length of L_{c1}, which is closer to the control point, should not be extremely small. Therefore, L_{c1} was set at 11/45R, 13/45R, 15/45R, 17/45R, and 19/45R for the hydrodynamic simulations, and the obtained results are shown in Fig. 9.

Figures 9(a), (b), and (c) present the variation patterns of the thrust coefficient, torque coefficient, and efficiency, respectively, of the mixed four-bar/five-bar cycloidal propeller with respect to L_{c1}. As shown, with variations in L_{c1}, these parameters fluctuate within a small range. Therefore, within the considered data range, the variations in the L_{c1} value does not significantly affect the thrust coefficient, torque coefficient, and efficiency of the mixed four-bar/five-bar cycloidal propeller. However, Fig. 9(d) shows that with increasing L_{c1} length, the velocity difference within one cycle after stabilization of the underwater vehicle increases significantly, especially when L_{c1} = 17/45R or 19/45R, the magnitude of velocity difference is noticeably larger. Therefore, considering the smooth navigation of the watercraft, a smaller length for L_{c1} is recommended.

3.3 Comparison Between the Hydrodynamic Performances Of Four-Bar and Mixed Four-Bar/Five-Bar Cycloidal Propellers

This section presents the comparison between the hydrodynamic performances of the closely sized four-bar and mixed four-bar/five-bar cycloidal propellers under stable cruising conditions. Considering the actual dimensions of the cycloidal propeller in this study, the available power from the driving motor was limited, and the actual stable operating speed underwater was approximately 5 rps. Therefore, for the four-bar mechanism (with linkage lengths of $L_a = R$ = 45 mm, L_b = 2/9R = 10 mm, $L_c = R$ = 45 mm, L_d = 11/45R = 11 mm) and the four-bar/five-bar mechanism (with linkage lengths of $L_a = R$ = 45 mm, L_b = 2/9R = 10 mm, L_{c1} = 11/45R = 11 mm, L_{c2} = 34/45R = 34 mm, L_d = 11/45R = 11 mm), the cycloidal propellers are subjected to a revolution speed of 5 rps, and then compared horizontally in terms of thrust coefficient, torque coefficient, efficiency, and velocity difference after reaching the steady-state navigation phase, as shown in Table 3.

Table 3 Comparison between the hydrodynamic performances of the four-bar and mixed four-bar/five-bar cycloidal propellers

Performance parameter	Four-bar	Mixed four-bar/five-bar
Thrust coefficient K_F	0.6912	1.3178
Torque coefficient K_M	2.2090	3.3066
Efficiency η	0.2608	0.3621
Velocity difference ΔV (m/s)	0.0138	0.0286

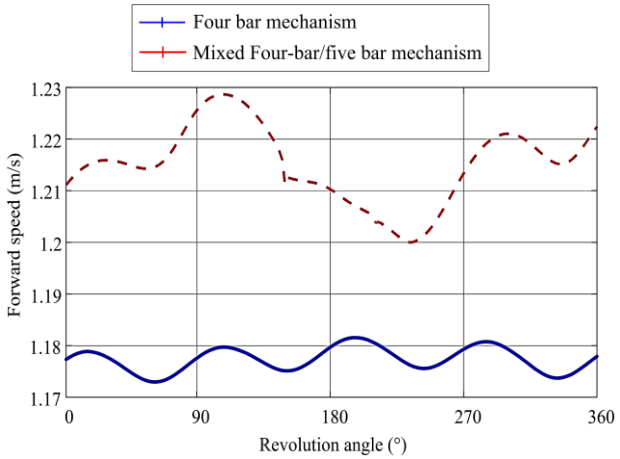

Fig. 10 Comparison of forward velocities within a single cycle for the four-bar and mixed four-bar/five-bar cycloidal propellers

We compared the hydrodynamic performance parameters of the four- and mixed four-bar/five-bar cycloidal propellers at a revolution speed of 5 rps. As shown, compared to the mixed four-bar/five-bar cycloidal propeller, the thrust coefficient, torque coefficient, and efficiency of the four-bar cycloidal propeller has lower values. However, the vehicle equipped with the four-bar cycloidal propeller experiences smaller velocity difference within one cycle during steady-state navigation phase compared to the mixed four-bar/five-bar cycloidal propeller. The velocity variation curves within one cycle during steady-state navigation phase for the vehicle equipped with the four-bar and mixed four-bar/five-bar cycloidal propellers at a revolution speed of 5 rps are shown in Fig. 10. The vehicle equipped with the mixed four-bar/five-bar cycloidal propeller achieves a higher forward velocity. However, it also experiences larger velocity differences within a single revolution cycle. In other words, the mixed four-bar/five-bar cycloidal propeller generates greater thrust force but with larger fluctuations during each cycle. Therefore, for a higher thrust force, the mixed four-bar/five-bar cycloidal propeller must be used. However, if a smoother propulsion effect is preferred, the four-bar cycloidal propeller is recommended.

4. DISCUSSION

4.1 Influence of the Linkage Lengths on the Blade's Rotation Angle of the in the Four-Bar Cycloidal Propellers

The most direct effect of varying the lengths of the individual linkages in the four-bar and mixed four-bar/five-bar mechanisms on cycloidal propellers is the alteration of the rotational motion patterns of the blades about their own axis. Therefore, to determine the influence of linkage-length variations in the four-bar and mixed four-bar/five-bar mechanism on the hydrodynamic performance of cycloidal propellers, one must first analyze the impact of linkage-length variations on the blade-rotation angles.

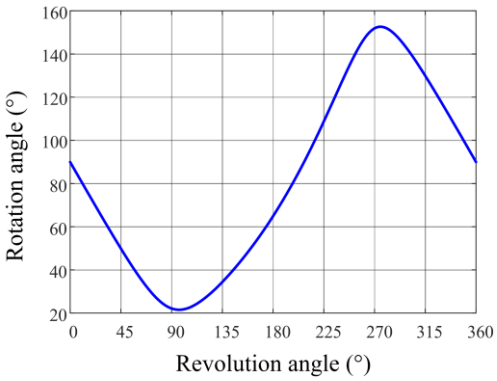

Fig. 11 Variation law of blade's rotation angle for a four-bar cycloidal propeller in a single cycle

In a four-bar cycloidal propeller, the rotational angles of the four blades exhibit a waveform within one cycle that resembles a sinusoidal curve with a phase difference of $\pi/2$. Therefore, by plotting the variation curve of the rotation angle for any one blade throughout a cycle, the variations in the rotation angles of all blades can be obtained. For example, consider a four-bar mechanism with linkage lengths of $L_a = R = 45$ mm, $L_b = 2/9R = 10$ mm, $L_c = R = 45$ mm, and $L_d = 11/45R = 11$ mm; then, the rotation angle curve of a blade within one cycle is shown in Fig. 11.

Within each cycle, the curve of the blade's rotation angle follows a pattern similar to a sinusoidal curve. For the aforementioned linkage lengths, the variation range for the blade's rotation angle is between 21.52° and 152.6°, with the equilibrium position at 89.94°. By using a similar approach, we plotted the curves of a blade's rotation angle variation within one cycle for all combinations of linkage lengths of L_b and L_c. As observed, all the curves exhibited a similar sinusoidal pattern. However, the amplitudes of the angle variations and equilibrium positions differ depending on the variations in L_b and L_c. The variation range and equilibrium positions for the blade's rotation angle obtained by changing L_b and L_c are shown in Fig. 12, and the fitted-plane equations are provided in Table 4.

As shown in Fig. 12, an increasing L_b results in a significant increase in the amplitude of blade's rotation. Within the dimensions selected for this study, an increase of L_b by $1/45R = 1$ mm results in an approximate 20° increase in the blade's rotation amplitude. Similarly, the increase in L_c gradually increases the equilibrium position angle of the blade's rotation. Within the dimensions selected for this study, an increase of L_c by $4/45R = 4$ mm results in an approximate 20° increase in the equilibrium position angle of the blade's rotation. Based on the aforementioned discussions, the increases in L_b and L_c result in the expansion of the range of blade rotation and an increase in the equilibrium position angle of blade rotation, respectively, which, in turn, enhance the thrust coefficient, torque coefficient, and efficiency of the cycloidal propeller. However, the impact of this increase is not as significant as the variation in blade-rotation amplitude.

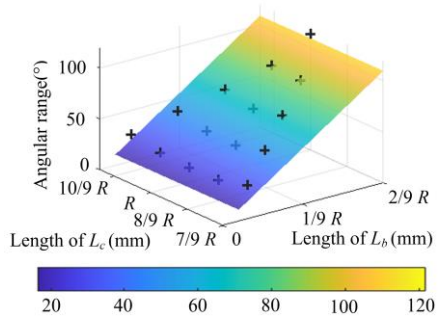

(a) Variation of angular range with respect to the length of L_b and L_c

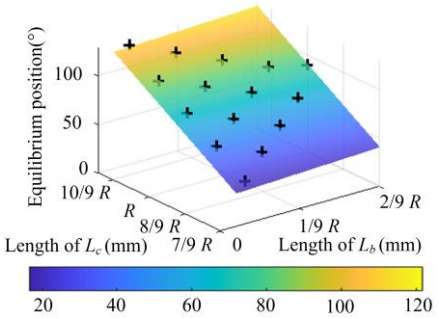

(b) Variation of equilibrium position with respect to the length of L_b and L_c

Fig. 12 Variation of (a) angular range and (b) equilibrium position of the four-bar cycloidal propeller with respect to the length of L_b and L_c

Table 4 Data point fitting plane equation for the data in Fig. 12

Figure number in Fig. 12	Angular parameter	Fitting plane equations
Fig. 12(a)	Angular range	$z = 10.94x - 0.04712y + 2.097$
Fig. 12(b)	Equilibrium position	$z = 0.7082x + 5.049y - 143.3$

For a unit length of the blade, let C_L and C_D represent the lift and drag coefficients of the blade profile, respectively, d denote the chord length of the blade, and V_R represent the resultant velocity of the blade motion. In a medium with density ρ, the lift F_L and drag F_D acting on this segment of the blade can be expressed as follows:

$$F_L = C_L \frac{\rho}{2} V_R^2 d \tag{15}$$

$$F_D = C_D \frac{\rho}{2} V_R^2 d \tag{16}$$

As shown, the medium density and blade chord length were taken as constant in this study. The lift and drag coefficients of the blade vary with respect to the angle of attack of the blade. The resultant velocity of the blade motion is influenced by the blade's revolution speed and rotation speed. By using Eq. (15) and Eq. (16), the relationship between the rotation pattern of the blade and the magnitude of lift and drag produced by a unit length of the blade can be established. The integration of the lift and drag of a unit length of the blade yields the total lift and drag generated by each blade. If the interaction between the blades is not considered, the propulsive force and torque of the cycloidal thruster can be approximated as the vector sum of forces acting on multiple blades.

As shown in Eq. (15) and Eq. (16), the lift and drag of a unit length of the blade are positively correlated with the square of the resultant velocity, V_R, of the blade relative to the incoming flow. Further, the resultant velocity of the blade is obtained by vector addition of the blade's revolution velocity, rotation velocity, and relative velocity of the incoming flow. In this study, the revolution speed of the cycloidal thruster was set constant at 5 rps during the numerical simulation of the blade's dimensions, L_b and L_c. Therefore, in each dataset, the revolution speed of the blade at the same revolution position is identical in magnitude and direction. Although the relative velocities between the propeller in self-propulsion and the stationary water flow vary, their differences compared to the velocities generated by blade revolution and rotation can be neglected. Hence, the variation in the resultant velocity, V_R, of the blade can be approximated as primarily influenced by the angular velocity of blade rotation. As shown in Fig. 12(a), within the same revolution period, a larger amplitude of the rotation angle requires a corresponding increase in the rotation angular velocity. Therefore, the influence of L_b variation on the hydrodynamic performance of the cycloidal propeller can be summarized as follows: increasing L_b expands the range of the rotation angle of the blade within a single cycle, allowing the blade to achieve a greater angular velocity of rotation within the same revolution cycle. This, in turn, increases the resultant velocity of blade motion, thus enhancing the lift and drag generated by the unit length of the blade, and ultimately improving the overall coefficients of thrust and torque of the cycloidal propeller.

Different rotation-angle patterns of the blade's rotation will also alter the angle of attack relative to the incoming flow at the same revolution position, which in turn affects the lift and drag coefficients of the blade in Eq. (15) and Eq. (16). The angle of attack of the blade is determined by the blade's revolution angle, rotation angle, and the relative angle between the blade and incoming flow. When the revolution position is the same, the magnitude of the attack angle is also primarily governed by the rotation angle. As shown in Fig. 12(b), increasing the length of L_c elevates the equilibrium position of the rotation angle of the blade without changing its amplitude, thereby altering the angle of attack. However, the relationship between the lift coefficient, drag coefficient, and attack angle is relatively complex and non-monotonic. When the angle of attack increases considerably, the phenomenon may be stalled. Therefore, the variation pattern and stall angle are closely related to the blade's shape. Therefore, the impact of changes in the equilibrium position of the rotation angle of the blade on the hydrodynamic performance of the cycloidal propeller is not straightforward. According to the aforementioned numerical simulation results, the increase of the length of L_c significantly raises the equilibrium position of the

Table 5 Range, amplitude, and equilibrium position of blade rotation angle under different L_d values

L_d (mm)	Angular range (°)	Amplitude (°)/ Equilibrium position (°)
11	21.52–152.60	131.08/89.94
12	29.07–142.40	113.33/89.79
13	34.09–135.30	101.21/89.56
14	37.77–129.60	91.83/89.27
15	40.60–125.00	84.40/88.94

blade's rotation angle, consequently altering the angle of attack. However, this only results in a minor improvement in the coefficients of thrust and torque of the cycloidal propeller.

Note that owing to the combined effect of the blade's rotation, revolution, and relative motion with respect to the water flow, it is not possible to accurately calculate the lift, drag, thrust coefficient, and torque coefficient of the blade or the cycloidal propeller solely based on the rotation angle and angular velocity. However, in the numerical simulations conducted with the same set of parameters for the revolution speed and phase, the obtained rotation angle curves show similar shapes. Under this premise and by comparing the rotation angular velocities, we can achieve a qualitative comparison of the hydrodynamic performance of the cycloidal propeller based on the blade element theory.

We further studied the influence mechanism of the variation in linkage length, L_d, on the coefficients of thrust and torque of the cycloidal propeller. In Section 3.1, numerical simulations were conducted with different values of L_d, resulting in similar curves for blade rotation angle. However, the range of rotation angle and the equilibrium position differ, as presented in Table 5.

Table 5 shows that as L_d increases, the range of blade-rotation angles within one revolution significantly decreases and the equilibrium position slightly decreases. Consequently, the thrust and torque coefficients of the cycloidal propeller significantly decrease with the increase in L_d; this result is consistent with the results obtained from numerical simulations.

4.2 Influence of the Linkage Lengths on the Blade's Rotation Angle for the Mixed Four-Bar/Five-Bar Cycloidal Propellers.

Based on the discussion about the influence of linkage-length variation on blade rotation and hydrodynamic performance of a four-bar mechanism cycloidal propeller, this section provides an analysis on the effect of linkage-length variation on blade rotation angle and hydrodynamic performance in a mixed four-bar/five-bar mechanism cycloidal propeller. According to the modeling presented in Section 2.2, the rotation patterns of the four blades in the mixed four-bar/five-bar cycloidal propeller were influenced by the geometric structure of the crossbar owing to mechanical reasons. Each blade has a distinct rotation pattern, and Fig. 13 shows the curves depicting the variation of blade rotation during one cycle for different L_{c1} values selected for numerical simulations in this study.

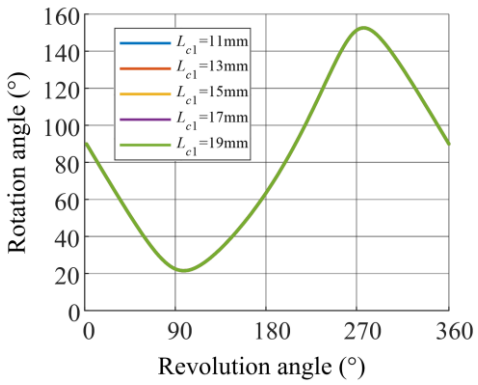

(a) Variation law of the rotation angle for blade 1

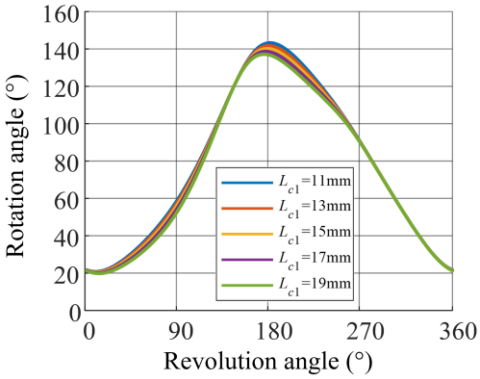

(b) Variation law of the rotation angle for blade 2

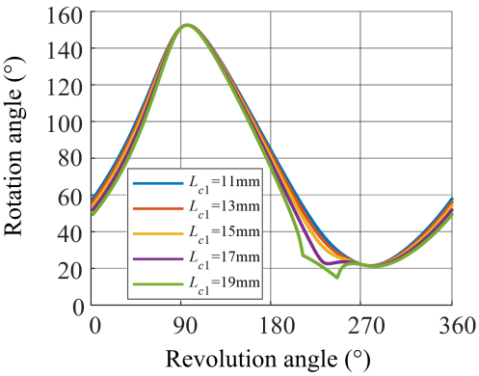

(c) Variation law of the rotation angle for blade 3

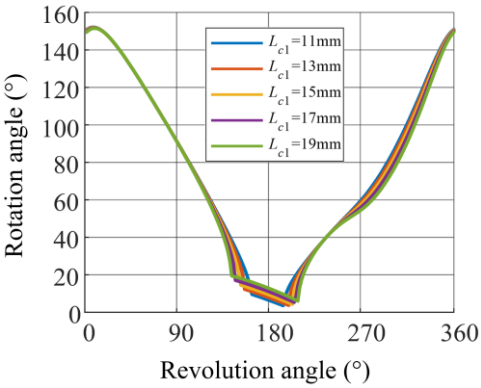

(d) Variation law of the rotation angle for blade 4

Fig. 13 Variation curve of the rotation angle of each blade of the mixed four-bar/five-bar cycloidal propeller with different L_{c1} lengths

As shown in Fig. 13, an increase in the L_{c1} length minimally effects the amplitude of blade deflection and equilibrium position during one cycle. Based on the previous discussion, changes in the L_{c1} length would not significantly affect the coefficients of thrust and torque of the cycloidal propeller. This observation is further supported by the conclusions obtained from the numerical simulations presented in Section 3.2.

Figure 13 shows that blade 4 exhibits an abrupt change in its rotation angle near a revolution angle of 180°, which is not observed in the four-bar mechanism of the cycloidal propeller. This irregularity is caused by a singularity occurring at the connection between the L_{c1} portion of the five-bar mechanism and connecting bar L_{c2}. As the L_{c1} length increases, an irregular change occurs at an earlier time point in the rotation angle of blade 4. When the length of L_{c1} exceeds 17/45R, blade 3 exhibits a similar irregular change. This irregular transition inevitably results in a sudden change in the blade's angular velocity, resulting in increased thrust variation and velocity difference within one cycle. This observation aligns with the results obtained from numerical simulations in Sections 3.2 and 3.3, indicating that the velocity differences within one cycle of the five-bar mechanism increase with the length of L_{c1}. Overall, the velocity differences in the five-bar mechanism are greater than those in the four-bar mechanism.

4.3 Difference in the Hydrodynamic Performances of a Four-Bar and Mixed Four-Bar/Five-Bar Cycloidal Propellers

Under the same revolution speed, we compared the four-bar cycloidal propeller comprising parameters $L_a = R$ = 45 mm, L_b = 2/9R = 10 mm, $L_c = R$ = 45 mm, and L_d = 11/45R = 11 mm with the mixed four-bar/five-bar cycloidal propeller comprising parameters $L_a = R$ = 45 mm, L_b = 2/9R = 10 mm, L_{c1} = 11/45R = 11 mm, L_{c2} = 34/45R = 34 mm, and L_d = 11/45R = 11 mm. The ranges, amplitudes, and equilibrium position of the blade's rotation within a single revolution period for both cases are shown in Table 6. Under these parameters, the rotation amplitude of blade 1 in the mixed four-bar/five-bar mechanism is the same as that in the four-bar mechanism. Blade 3 exhibits a similar rotation amplitude to the four-bar mechanism, whereas blade 2 has a slightly smaller amplitude. In contrast, Blade 4 has a significantly larger rotation amplitude than that of the four-bar mechanism. Therefore, under the same revolution speed, the thrust and torque coefficients of the four-bar cycloidal propeller with the aforementioned parameters are slightly smaller than those of the mixed four-bar/five-bar cycloidal propeller. The numerical simulation results in Section 3.3 strongly support the validity of the aforementioned discussion.

Based on the numerical simulation results and discussions, we can conclude that in a series of cycloidal propellers developed based on the four-bar mechanism, the key to altering the hydrodynamic performance of the cycloidal propeller lies in modifying the range and equilibrium position of the blade's rotation. Changes in the mechanism's structure (from a four-bar to a mixed four-bar/five-bar) or alterations in the mechanism's parameters (such as modifying the linkage lengths) results in variations in the shape of the blade's rotation curve. However, if these changes do not affect the range and equilibrium position of the blade's rotation curve, their impact on the coefficients of thrust and torque of the cycloidal propeller is limited along with their influence on efficiency.

4.4 Impact of a Blade's Rotation Angle Variations within One Cycle on the Hydrodynamic Performance of the Cycloidal Propellers

In this section, we consider blade 4 of a mixed four-bar/five-bar mechanism cycloidal propeller as an example with the following linkage lengths: $L_a = R$ = 45 mm, L_b = 2/9R = 10 mm, L_{c1} = 11/45R = 11 mm, L_{c2} = 34/45R = 34 mm, and L_d = 11/45R = 11 mm. Then, the influence of the variation in blade angles during stable self-propulsion of the underwater vehicle on the hydrodynamic performance of the cycloidal propeller is discussed. Figure 14 presents the variation curves of the rotation angular velocity and resultant force generation of blade 4 within one cycle during stable uniform propulsion of the self-propulsion cycloidal propeller. The horizontal axis represents the revolution angle. Additionally, transient pressure distribution was observed around the cycloidal propeller blade during different discrete moments within the cycle. As shown in Fig. 15, the six dotted lines represent the pressure distribution cloud diagrams at selected angles with an interval of 60°. In addition, the revolution angles

Table 6 Range, amplitude, and equilibrium position of blade rotation angle of the four-bar and mixed four-bar/five-bar cycloidal propellers

Cycloidal propeller mechanism		Angular range (°)	Amplitude (°)/ Equilibrium position (°)
Four-bar		21.52–152.6	131.08/89.94
Mixed four-bar/five-bar	Blade1	21.52–152.60	131.08/89.94
	Balde2	22.67–143.19	120.52/-
	Blade3	21.43–152.60	131.17/-
	Blade4	3.58–152.10	148.52/-

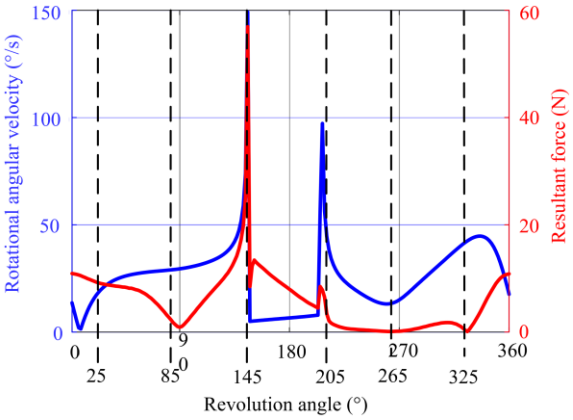

Fig. 14 Comparison of rotational angular velocity and resultant force of blade 4 within a single cycle

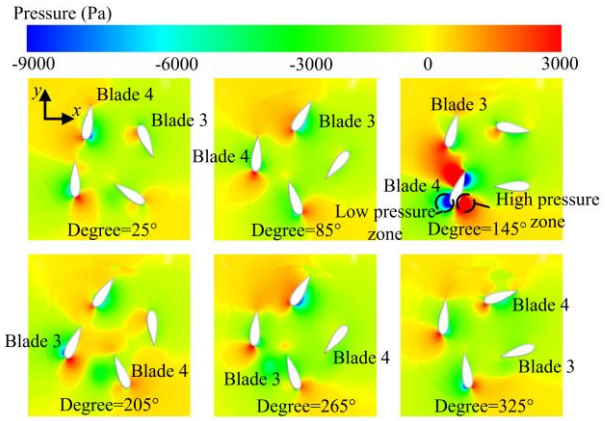

Fig. 15 Cloud chart of blade pressure of the mixed four-bar/five-bar cycloidal propeller

corresponding to the discrete moments are indicated with degrees.

The force exerted on an individual blade is generated according to the pressure difference between the inner and outer sides of the blade. As shown in Fig. 15, the blade displays a low-pressure region on one side and a high-pressure region on the other side. The greater the pressure difference between the low- and high-pressure regions, the greater is the force exerted on the blade. The combined force of the four blades is the propulsion force of the cycloidal propeller. As shown in Fig. 14, the magnitude of the resultant force of blade 4 can be well approximated by the pressure difference between the inner and outer sides of the blade, as shown in the corresponding pressure cloud diagram in Fig. 15. Therefore, the propulsion force of the cycloidal propeller blades can be qualitatively assessed based on the pressure cloud diagram.

The comparison of the curves in Fig. 14 evidently shows that when the revolution angle reaches 145°, blade 4 undergoes a sudden transition in its rotational swing, resulting in a significant peak in its angular velocity. Consequently, the resultant force acting on blade 4 also exhibits a peak. This observation is further supported by Fig. 15, which clearly shows a pronounced pressure difference between the inner and outer sides of blade 4 at a revolution angle of 145°.

However, note that in Fig. 14, the rotation angular velocity of the blade does not fully correspond to the resultant force acting on the blade. The relationship between the blade's rotation angle and the revolution position, as depicted through the discrete pressure cloud map (Fig. 15), indicates that the relative angle of attack and velocity of the blade with respect to the water flow depend not only on the blade's rotation angle and angular velocity but also on the revolution position and water-flow direction. Additionally, the resultant thrust produced by the cycloidal propeller is a composite of multiple blades, and interactions exist among the blades themselves. The synthesis of thrust from multiple blades further complicates the accurate calculation of the total thrust of the cycloidal propeller. Therefore, the proposed relationship between the amplitude of the blade's rotation and the thrust and torque of the cycloidal propeller is primarily applicable for qualitatively estimating the average hydrodynamic performance over multiple cycles for a group of cycloidal propellers with similar rotation pattern curves within a certain range. For calculating the instantaneous hydrodynamic performance of the cycloidal propeller in specific cases, such as transient simulations, CFD, or other similar methods must be employed to obtain accurate numerical results.

5. CONCLUSION

This study models and conducts numerical simulations on a four-bar and mixed four-bar/five-bar cycloidal propeller in the auto-propulsion mode, with multiple sets of linkage lengths variations. This study applied the wing element theory to analyze the effects of linkage-length variations in four-bar and mixed four-bar/five-bar configurations on the hydrodynamic performance of the propeller. Furthermore, the research elucidates the relationship between linkage-length variations and hydrodynamic performance of the cycloidal propeller in the auto-propulsion mode, and the underlying mechanisms were analyzed. Additionally, this paper presents a method for estimating the hydrodynamic performance of the cycloidal propeller based on blade rotation. The main conclusions of this study are as follows:

(1) For the four-bar cycloidal propeller, following the linkage naming convention provided in this paper:

- The length of linkage L_a determines the rotational radius of the cycloidal propeller and should be chosen based on the actual installation dimensions of the vehicle.

- The length of linkage L_b increases the rotation amplitude of the blades. Considering the thrust coefficient and efficiency, a relatively longer L_b should be selected. However, an increase in L_b slightly increases speed fluctuations.

- The length of linkage L_c raises the equilibrium position of blade rotation in the cycloidal propeller. In terms of thrust coefficient and efficiency, a relatively longer L_c should be chosen. However, the impact of increasing L_c is not as significant as that of L_b.

- The length of linkage L_d reduces the rotation amplitude of the blades. Considering thrust coefficient and efficiency, a relatively shorter L_d should be selected. However, a decrease in L_d slightly increases speed fluctuations.

(2) Based on the conclusions in (1), for the mixed four-bar/five-bar cycloidal propeller, length variations of L_{c1} do not exert a significant influence on the rotation amplitude and equilibrium position of the blades. The thrust coefficient, torque coefficient, and efficiency of the cycloidal propeller also do not exhibit significant changes with variations in L_{c1}.

(3) At the same rotational speed, the mixed four-bar/five-bar cycloidal propeller is advantageous in that its displays better thrust coefficient and efficiency. However, in terms of navigation stability, the four-bar cycloidal propeller outperforms the mixed propeller.

(4) Within a set of similar multilinkage cycloidal propellers, variations in linkage lengths affect the hydrodynamic performance of the cycloidal propeller by altering blade-rotation angular range and equilibrium position. The thrust coefficient, torque coefficient, and efficiency of the propeller increase with a larger blade-rotation angular range and higher equilibrium position. Notably, the impact of blade-rotation angular range is more pronounced.

In a future study, we plan to improve the hydrodynamic performance of the cycloidal propeller, design a more reasonable blade-rotation curve, and develop a corresponding control mechanism.

ACKNOWLEDGEMENTS

This work was supported by National Natural Science Foundation of China [grant number 51875101], and State Key Laboratory of Robotics and System (HIT) [grant number SKLRS-2018-KF-11]. The authors greatly appreciate the referees for their helpful comments and suggestions, which help improve this paper.

CONFLICT OF INTEREST

The authors declare that they have no known competing financial interests or personal relationships that could have appeared to influence the work reported in this paper.

AUTHORS CONTRIBUTION

H. Yan: Conceptualization, Methodology, Formal analysis, Writing - Original Draft; **Z. Zhou**: Software, Validation, Investigation, Data Curation; **M. Lei**: Supervision, Visualization; **Z. Li**: Project administration; **D. Xia**: Writing - Review & Editing, Funding acquisition

REFERENCES

Amin, S., Mohammad, A. B., Hafiz, M. A. (2023). Comprehensive evaluation of the entropy generation in oval twisted double-pipe heat exchanger using non-Newtonian nanofluid using two-phase mixture model. *Engineering Analysis with Boundary Elements*, *152*, 637-644. https://doi.org/10.1016/j.enganabound.2023.04.021.

Andrisani, A., Angeli, D., Dumas, & Antonio. (2016). Optimal pitching schedules for a cycloidal rotor in hovering. *Aircraft Engineering & Aerospace Technology*. *88*(5), 623–635. https://doi.org/10.1108/AEAT-02-2015-0066.

Bakhtiari, M., & Ghassemi, H. (2019). A 2.5D numerical study on open water hydrodynamic performance of a Voith-Schneider propeller. *Mechanics & Industry*, *20*(6) 617. https://doi.org/10.1051/meca/2019049

Bakhtiari, M., & Ghassemi, H. (2020). CFD data based neural network functions for predicting hydrodynamic performance of a low-pitch marine cycloidal propeller. *Applied Ocean Research*, *94*, 101981. https://doi.org/10.1016/j.apor.2019.101981

Bertram, V. (2012). *Practical ship hydrodynamics* (*Second Edition*). Elsevier. https://doi.org/10.1016/C2010-0-68326-X

Brockett, T. (1991, 17-18 September). *Hydrodynamic analysis of cycloidal propulsors* [Conference session]. Propellers/Shafting 91 Symposium, Virginia Beach, VA, United States.

Desai, M., Gokhale, R., Halder, A., Benedict, M., & Young, Y. L. (2020). Augmenting Maneuverability of UUVs with Cycloidal Propellers. *Preprints*. https://doi.org/10.20944/preprints202005.0434.v1

Hafiz, M. (2023). Thermal management systems for batteries in electric vehicles: A recent review. *Energy Reports*, *9*, 5545-5564. https://doi.org/10.1016/j.egyr.2023.04.359.

Hu, J., Yan, Q., Ding, J., & Sun, S., (2022), Numerical study on transient four-quadrant hydrodynamic performance of cycloidal propellers. *Engineering Applications of Computational Fluid Mechanics*, *16*(1), 1813-1832. https://doi.org/10.1080/19942060.2022.2118171

Hu, Y., Fu, X., Zhang, H. L., Wang, G. Q. & Farhat, H. (2019). Effects of blade aspect ratio and taper ratio on hovering performance of cycloidal rotor with large blade pitching amplitude. *Chinese Journal of Aeronautics*. *32*(5), 1121-1135. https://doi.org/10.1016/j.cja.2019.01.015

Isay, W. H. (1968). Zur Theorie des Voith-Schneider-Propellers. *Ingenieur-Archiv*, *37*, 125–140. https://doi.org/10.1007/BF00532712

Jakson, A. L. M., & José, P. (2018). *Effects of harmonic vibration on cycloidal rotor performance*, [Conference session]. ASME 2018 International Mechanical Engineering Congress and Exposition 2018, Pittsburgh, USA. https://doi.org/10.1115/IMECE2018-87103

Ju, Y., Babaei-Mahani, R., Ibrahem, R. K., Khakberdieva, S., Karim, Y. S., Abdalla, A. N., Mohamed, A., Mahmoud, M. Z. & Ali, H. M., (2022). Discharge enhancement in a triple-pipe heat exchanger filled with phase change material. *Nanomaterials*, *12*(9), 1605. https://doi.org/10.3390/nano12091605

Jürgens, D., Palm, M., Singer, S., & Urban, K. (2007). Numerical optimization of the Voith-Schneider Propeller. *Journal of Applied Mathematics and Mechanics*, *87*(10), 698–710. https://doi.org/10.1002/zamm.200510345

Kirsten, J. (1922). Propeller. *US*, *1432700*. https://patents.google.com/patent/US1432700

Li, Z., Xia, D., & Zhou, Z. (2023). The role of double-tentacled cooperative kinematics on the hydrodynamics of a self-propelled swimmer. *Journal of Applied Fluid Mechanics*, *16*(6), 1193-1207. https://doi.org/10.47176/jafm.16.06.1547

Manen, J. V. (1966). Results of systematic tests with vertical axis propellers. *International shipbuilding progress, 13*, 382-398. https://doi.org/10.3233/ISP-1966-1314802

Qian, X. N. (1963). Performance Analysis and Theory of Straight Wing Propulsion. *China Shipbuilding.* (03): 11-27. https://doi.org/ CNKI:SUN:ZGZC.0.1963-03-001.

Qin, D. H., Pan, G., Lee, S., Huang, Q., & Shi, Y. (2019). Underwater radiated noise reduction technology using sawtooth duct for pump-jet propulsor. *Ocean Engineering*, *188*(9), 1−15. https://doi:10.1016/j.oceaneng.2019.106228

Raj, A., & Thakur, A. (2016). Fish-inspired robots: Design, sensing, actuation, and autonomy—a review of research. *Bioinspiration & Biomimetics*, *11*(3), 031001. https://doi:10.1088/1748-3190/11/3/031001

Shi, L., Bayeul-Lainé, A. C., & Coutier-Delgosha, O. (2022), Numerical investigations on unsteady vortical flows and separation-induced transition over a cycloidal rotor at low Reynolds number, *Energy Conversion and Management*, *266*, 115812. https://doi.org/10.1016/j.enconman.2022.115812

Valentini, P. (2001). *Vertical axis and transversal flow nautical propulsor with continuous self-orientation of the blades. US, US06244919B1*.

Voith Group (2021). *Precise and safe maneuvering: Voith Schneider Propeller*. https://d2euiryrvxi8z1.cloudfront.net/asset/445934742530/85785d8de54ef5402095017f6789f347/vt2070-english.pdf

Laucks, R., & Blickle, K. (1983). Amphibious Vehicle. *US, 4419085*.

Voith Gmb, H. & Co. KGa A. (2019, September 19). Voith scneider propellers. http://www.voith.com/ca-en/products-services/power-transmission/voith-schneider-propeller-10002.html

Walther, C. M., Saemi, F., Benedict, M. & Lakshminarayan, V. (2019). Symmetric versus asymmetric pitching of a cycloidal rotor blade at ultra-low reynolds numbers. *Journal of Aircraft*, *56*(3). 1179-1199. https://doi.org/10.2514/1.C034776

Wheatley, J. B., & Windler, R., (1935). *Wind-tunnel tests of a cyclogiro rotor*. National Advisory Committee for Aeronautics Technical Note No. 528. https://ntrs.nasa.gov/citations/19930081270

Yu, H., Beng, T. W., & Bin, L. K. (2003). *The analysis of cyclogyro using Unsteady Vortex Lattice Method* [Conference session]. ICAS-Secretariat - 25th Congress of the International Council of the Aeronautical Sciences 2006, Hamburg, Germany.